Journal of the Royal Society Interface: Electronic Supplementary Material, February 2020

Three-dimensional wing structure attenuates aerodynamic efficiency in flapping fly wings

Thomas Engels[1,2], Henja-Niniane Wehmann[2], and Fritz-Olaf Lehmann[2*]

1 LMD-CNRS, École Normale Supérieure and PSL, Paris, 24 rue Lhomond, 75231 Paris Cedex 05, France

2 Department of Animal Physiology, University of Rostock, Rostock, Albert-Einstein-Str. 3, 18059 Rostock, Germany

* Email of corresponding author: fritz.lehmann@uni-rostock.de

1. Body morphometrics and wing kinematics

Introduction

Stroke kinematic patterns in flies are not constant but vary during manoeuvring flight. Studies on wing kinematics in freely flying fruit flies, for example, show that flies dynamically adjust wing kinematics to control all axes of rotation and thus yaw, pitch, and roll moments [1-3]. The kinematic modifications are mostly small but pronounced during more extreme manoeuvres such as take-off behaviour and saccadic flight turns [3-5]. Kinematic changes in Diptera are largely due to changes in neural activity of flight steering muscles that modify the transmission of power from asynchronous flight muscles to the wings [6-8]. Tethered flight studies have shown that the activity of basalar and axillary steering muscles are correlated with distinct changes in downstroke deviation angles and stroke plane. In *Calliphora vicina*, for example, co-activation of sternobasalar muscle M.b2 and a phase advance of first basalare M.b1 converts a figure-8 into an O-shaped wing tip trajectory pattern [9]. Similar kinematic alterations are also reported by previous studies on tethered flying *Phormia regina* [10].

As wing kinematics is not a constant, there is not a single kinematic pattern that characterizes flight in a fly *per se*. All numerical simulations that use repetitive stroke kinematics are limited in this respect and thus highlight only a fraction of all possible flow conditions and forces during flight. It is evident that modifications in wing kinematics change flow structures at flapping wings and in the wake, and thus the production of forces and moments. Nevertheless, we should consider all kinematic patterns within the kinematic envelope of a fly as a valid input for numerical and physical modelling of fly flight aerodynamics.

One aim of the present study is to demonstrate how lift capacity of corrugated and cambered wings depends on Reynolds number and thus size scaling. To compare differently-sized flies, it is necessary to use the same kinematic pattern for all tested species. Otherwise the measured differences may result from differences in wing kinematics rather than from changes in Reynolds number. According to previously measured stroke kinematics, stroke plane angles and maximum flight speeds, we generated a kinematic pattern for modelling that incorporates all typical kinematic features found in the three tested fly species (Table S1).

Stroke frequency, stroke amplitude, timing of wing rotation, and angle of attack

During tethered flight conditions, mean stroke frequency in *Calliphora* varies between ~127 Hz and ~180 Hz (mean ~158 Hz, [11]) and between ~120 Hz and ~160 Hz [9, 12]. In free flight, these frequencies range from ~117 Hz to ~158 Hz [13]. In *Musca* and *Drosophila,* studies on free flight performance reported stroke frequencies from ~147 Hz to ~170 Hz [14] and ~131 Hz to ~201 Hz [1,

15-16], respectively. Stroke amplitude considerably varies in flies, ranging from ~123° to ~160° in *Calliphora* , ~85° to ~140° in *Musca* [14] and ~136° to ~180° in tethered and freely flying *Drosophila* [2, 13, 17-18]. We used a mean value of 135° amplitude (Table S1).

We adopted the timing of wing rotation at the stroke reversals (0.22 stroke cycle) from previous measurements on *Calliphora* wing flapping at tethered flight conditions [19]. Rotational timing in freely manoeuvring *Drosophila* is similar and amounts to approximately 0.24 stroke cycle [2]. The wings' geometrical angle of attack (AoA) changes throughout the stroke cycle and depending on flight manoeuvres [3, 16-17]. Under tethered and free flight conditions, midstroke AoA in flies is typically higher during the downstroke than the upstroke [3-4]. Physical models mimicking fly flight used angles up to 45° during up- and downstroke [4-5, 20]. In the present study we adopted angles of attack from a previous study on elastic energy storage in flapping *Calliphora* wings [19], i.e. 40° during the downstroke and 20° during the upstroke.

Stroke plane

In our simulation, stroke plane was tilted nose-down (-20°) with respect to the horizontal for the following reason. In flies, mean flight force vector is orientated approximately normal to the wing's stroke plane [3, 21-22]. Thus, during forward flight, the stroke plane is typically tilted nose-down to allow thrust generation (Fig. 1). As *Drosophila* and *Musca* exhibit little change in mean stroke plane angle with respect to the longitudinal body axis (*Drosophila*, 24° vector orientation [23]), these species control the ratio between lift and thrust by changing their body inclination angle with respect to the horizontal [24]. A recent free flight study on *Drosophila* shows that the latter angle varies between ~20° and ~80° during manoeuvring flight and 40° and ~50° during forward flight [25]. At the latter body orientation, the fly's stroke plane is tilted nose-down by ~-20° with respect to the horizontal. We evaluated this value in freely flying *Musca domestica* using high-speed videography. We found an ~30° (nose-up) body inclination angle between the longitudinal body axis and the horizontal and ~30° - ~60° angle between longitudinal body axis and stroke plane. These values convert to ~-5° - ~-30° stroke plane angle with respect to the horizontal. In *Calliphora*, the stroke plane is tilted nose-down by ~-41.5° ±7° with respect to the longitudinal body axis [9]. As the longitudinal body axis is only aligned with the horizontal at maximum forward speed, stroke plane angle should be less at flight speeds below maximum. We evaluated this assumption by freely flying *Calliphora vomitoria* and measured stroke plane angle and forward speed at single wing strokes (N=6 flight sequences, n=28 stroke cycles). At a flight speed of 0.26 ms^{-1} (median; 0.05 ms^{-1} minimum speed, 0.69 ms^{-1} maximum speed), body inclination with respect to the horizontal is ~25° - ~30° (nose up) and the angle between stroke plane and body longitudinal axis is ~45° - ~50°. Stroke plane angles with respect to the horizontal thus range from ~-40° (nose down) to ~31° (nose up). Median was ~-19°. According to the above results, we thus used a stroke plane angle of -20° for all tested species.

Simulated free stream velocity

While *Drosophila* is capable of hovering flight, the two larger species typically require some head wind for body weight support. To attribute flight force production to wing design and not to kinematics, we derived forward speed (free stream velocity u_∞) from wing tip velocity using a constant ratio of 0.2 (Table S1). This constant was derived from a study that scored maximum flight capacity in flies [25]. The study showed that freely flying *Drosophila* achieve maximum optomotor compensation in response to a moving visual environment at ~0.47 ms^{-1} forward velocity. This value corresponds to ~20% mean wing tip velocity during flapping motion (Table S1) and to ~50% maximum flight speed in *Drosophila* [25].

Maximum forward flight speed for *Musca* is 2.0 - 2.3 ms^{-1} and for *Calliphora* 2.7 ms^{-1} [26]. This converts to 1.0 - 1.15 ms^{-1} and 1.35 ms^{-1} half maximum speed, respectively. The latter value was also

found in a study on the typical flight cruising speed of freely flying *Calliphora*, i.e. 1.2 - 1.4 ms^{-1} [27]. Similar to *Drosophila*, 50% maximum flight speed in *Musca* and *Calliphora* is equal to a ~0.2 ratio between wing tip velocity and forward speed. Altogether, the above data suggest the ratio between wing tip velocity and maximum horizontal speed is similar in all tested species and thus independent of body size. Moreover, measurements in freely flying *Calliphora* have shown that ~50% maximum speed is used most frequently during flight [27]. Noteworthy, free stream velocity in the computational domain was constant throughout the simulation for all tested species.

Remaining values for the three species such as body weight were adopted from a previous study on insect wing shape [28], and wing length and chord from our μCT measurements. The position of the wing's rotational axis in *Drosophila* was the line between wing root and tip [29], a line 0.21 wing chord behind the leading edge in *Musca* [14], and a line 0.286 mean wing chord behind the leading edge in *Calliphora* (Fig. 2) [19].

Conventional Reynolds number *Re* for wing motion is typically calculated during hovering flight conditions. As the models were tested at forward speed, we included cruising speed u_∞ and calculated cruising flight Reynolds number Re_∞ from mean wing tip velocity u_{tip}, mean chord width c_m, and kinematic viscosity of air ν_{air}. (15.43 x10^{-6} m^2s^{-1}) as,

$$Re_\infty = (u_{tip} + u_\infty)c_m\nu_{air}^{-1}. \qquad \text{(eq. S1)}$$

In equation S1, wing velocity u_{tip} was calculated as $2\Phi nR$ with Φ the wing's stroke amplitude, n the stroke frequency and R the wing length (Table S1).

Table S1. Parameters used in the computational fluid dynamics simulation. Data are taken from our μCT measurements and the literature. [1)], adopted from [1, 16, 30]; [2)] adopted from [14] and own measurements; [3)], adopted from [9, 11-13, 19]; [4)], μCT measurements from this study; [5)], adopted from [28]; [6)], see text.

	Drosophila	*Musca*	*Calliphora*
Stroke frequency *n* (Hz)	210[1)]	170[2)]	150[3)]
Stroke amplitude Φ (degrees)	135[3)]	135[3)]	135[3)]
Angle of attack at midstroke (degree)	$40_{up}/20_{down}$[3)]	$40_{up}/20_{down}$[3)]	$40_{up}/20_{down}$[3)]
Timing of wing rotation (cycle time)	0.22[3)]	0.22[3)]	0.22[3)]
Wing length *R* (mm)	2.37[4)]	6.42[4)]	9.76[4)]
Mean wing chord c_m (mm)	0.74[4)]	2.23[4)]	3.02[4)]
Body mass *m* (mg)	1.2[5)]	17.9[5)]	59.3[5)]
Wing tip velocity u_{tip} (ms^{-1})	2.35	5.14	6.90
Hovering flight Reynolds number *Re*	114	743	1352
Cruising flight Reynolds number Re_∞	137	892	1623
Free stream velocity u_∞ (ms^{-1})	0.47	1.03	1.38
Cut-off wing thickness h_w (μm)	28[6)]	75[6)]	114[6)]

Geometric similarity of wings

Wing shape differs slightly among individuals of the three tested species. To estimate the variance of wing shape, corrugation and camber, we quantified geometric variance in 53 wings of the three species using an optical profilometer (VR-3000, Keyence Corporation, Osaka, Japan) [28]. To evaluate shape variance, we scored height *z* of the dorsal surface as a function of the in-plane coordinates *x*

and *y*, selected 4 characteristic points on each wing (Fig. S1), measured 4 distances between these points and normalized to wing size using an isometric scaling factor *S*, i.e.,

$$S = \frac{l_{1,2} / L_{1,2} + l_{1,3} / L_{1,3} + l_{2,3} / L_{2,3} + l_{2,4} / L_{2,4}}{4}, \qquad \text{(eq. S2)}$$

with $L_{i,ii}$ the mean distance between point *i* and *ii* of all tested wings und $l_{i,ii}$ the distances between points on the wing used in the simulation (Table S2, Fig. S1).

Table S2. **Wing shape analysis.** Normalised distances between points 1-4 (see Fig. S1). Means ±standard deviation; *N*, number of tested wings.

	N	$L_{1,2}$ (μm)	$L_{1,3}$ (μm)	$L_{2,3}$ (μm)	$L_{2,4}$ (μm)
Drosophila	16	1600 ±43	1102 ±23	813 ±31	946 ±32
Musca	18	3619 ±88	2666 ±69	2609 ±88	5039 ±146
Calliphora	19	4142 ±119	3221 ±119	4079 ±108	7561 ±175

Variability of wing contour is shown in figure S2. For this analysis, we calculated the outer contour of μCT-scanned wing as used in the simulation (Fig. S2, red), and the median (Fig. S2, blue) and quantiles (0.25, 0.75; Fig. S2, grey) of wings scanned with the optical profilometer. We found only small differences in wing shape in all species. Variability is largest at the position of alula and wing hinge that mainly results from different amounts of wax used for wing fixation. We also computed variance of wing roughness scoring mean wing height *z*(*x*,*y*). These data are shown in figure 1*e-g* of the main text.

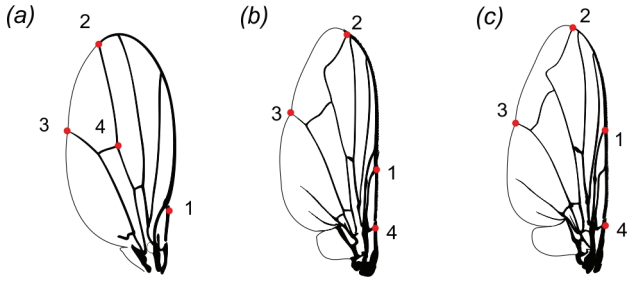

Figure S1. Characteristic points for shape analysis. Four points are selected to score wing shape in the three species (*a*) *Drosophila*, (*b*) *Musca*, and (*c*) *Calliphora*.

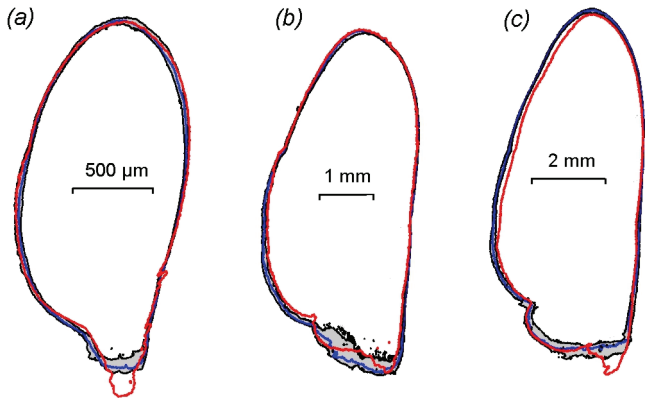

Figure S2. Variability of wing contour. Figure shows the contour of wings used in the simulations (red), the median contour of all tested wings of a species (blue), and 0.25 and 0.75 quantiles (grey shaded area). (*a*) *Drosophila*, *N*=16 wings; (*b*) *Musca*; *N*=18 wings; (*c*) *Calliphora*, *N*=19 wings.

2. Numerical setup

Our numerical code simulates a root flapping wing, using positional (ϕ), feathering (α) and deviation (θ) angles. The definition of kinematic angles follows a previously published study on bumble bee aerodynamics [31] and differs from definitions used in other insect flight studies, such as a study on wing elasticity in blowflies [19]. For non-flat wings, we defined wing position within its frame of reference, i.e. for ϕ, α, and θ equal to zero. This was achieved by manually defining a point of rotation at the wing base and computing a plane with smallest least mean square error to all surface points (bilinear regression). We assumed the same kinematics in both wings and thus simulated only the right wing.

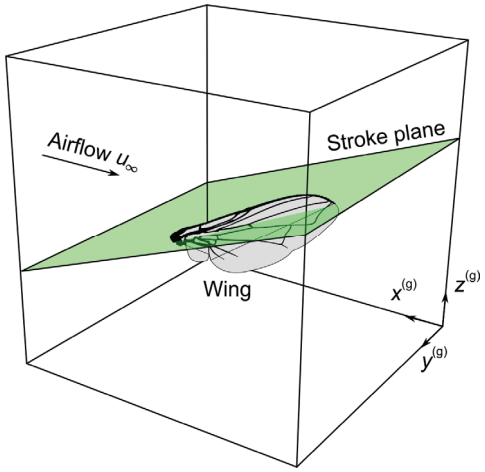

Figure S3. Global frame of reference for simulation. If not stated otherwise, stroke plane is tilted and free stream flow is horizontal during the numerical simulation.

3. Decomposition of wing structures

To separate camber from corrugation, we defined wing surface as a function $z_i(\underline{x})$ with $\underline{x} \in \Omega_w \subseteq \mathbb{R}^2$ for both the ventral ("bottom") and dorsal ("top") surfaces. Our definition formally excludes topologies like cavities and wing folding because in those cases z_i is not unique for a given $\underline{x}$. For thin, corrugated wings, this assumption is justified and did not introduce geometrical errors. We calculated the wing midplane $z_w(\underline{x}) = \frac{1}{2}(z_{top} + z_{bottom})$ from the sum of dorsal and ventral surfaces and the local thickness $h(\underline{x}) = z_{top} - z_{bottom}$ from the difference of both measures.

The aim of the following procedure was to decompose z_w into contributions from camber and corrugation. We defined corrugation z_{corr} as the high wave number part of z_w, while the remainder of the complementary low-pass filter is wing camber z_{cam}. The filter was selected according to the Fourier-spectrum of the wing surface (Fig. 2). The variable $z_w(\underline{x})$ is not suitable for conventional filters because it is only defined for Ω_w, which is a complex topology. To allow numerical filtering, we thus embedded $z_w(\underline{x})$ into the two dimensional periodic torus $\mathbb{T}^2$ and smoothly extended it to $\mathbb{T}^2 \setminus \Omega_w$. The extension was performed by solving a diffusion problem with the original data imposed as Dirichlet boundary condition. This was achieved by an iterative process that alternated between diffusing z and overwriting it in Ω_w by the original data (Fig. S4).

Filtering was performed in Fourier space, i.e. we first computed $\hat{z}(\underline{k}) = \mathcal{F}(z)$ using the fast Fourier transform (FFT). The filter kernel for corrugation was defined as:

$$g(\underline{k}) = exp\left[-\left((k_x - C_x)^2 + (k_y - C_y)^2\right)(2Q)^{-2}\right], \qquad \text{(eq. S3)}$$

with $k_i \in \mathbb{N}$, $0 \le k_i \le N_i$. The filter parameter Q was set to 10, derived from the FFT energy spectrum $E(k)$ of the natural wing. The energy spectrum is:

$$E(k) = \frac{1}{2} \sum_{k-\frac{1}{2} \le |\underline{k}| \le k+\frac{1}{2}} \left| \hat{z}_w(\underline{k}) \right|^2 . \qquad \text{(eq. S4)}$$

Within the energy spectrum, we identified two different slopes associated to camber and corrugation (Fig. 2d). The filter separated both contributions, i.e. $C_i = \frac{1}{2} N_i$.

Eventually, corrugation is equal to:

$$z_{corr} = \mathcal{F}^{-1}\left(g\hat{z}\right) \qquad \text{(eq. S5)}$$

and camber is:

$$z_{cam} = \mathcal{F}^{-1}\left((1-g)\hat{z}\right). \qquad \text{(eq. S6)}$$

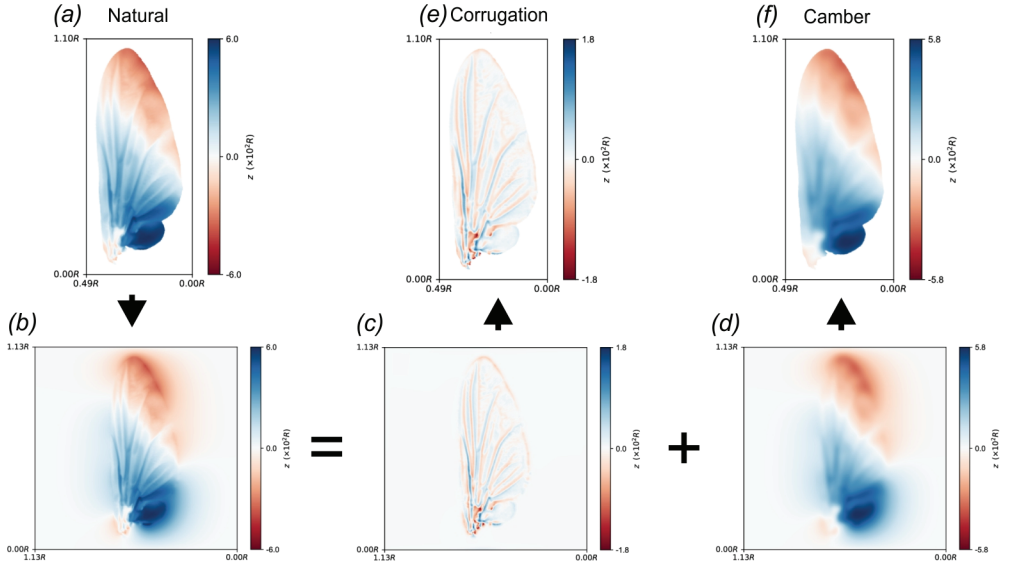

Figure S4. Decomposition of z in curvature and corrugation. (*a*) The original data (natural) were first embedded in a 2D torus. (*b*) We applied a smooth extension to solve the diffusion problem with Dirichlet boundary condition at the wing edges. The smoothed data were (*c*) high-pass and (*d*) low-pass filtered. The original data in *a* was used as a mask function to obtain (*e*) corrugation and (*f*) curvature of the wing.

4. Wing elasticity and fluid-structure-interaction

In our study, we tested the aerodynamic benefit of camber and corrugation and not the function of wing elasticity and deformation. Our wings were scanned while hydrated and attached to the fly body. This is different from many previous studies on insect wing aerodynamics and shows the wing free of deformation owing to desiccation. Camber and corrugation should thus be considered as “natural at rest”, at which the wing does not face any inertial or aerodynamic forces. Although adding wing flexibility or using predescribed kinematics may change the distribution and magnitude of inertial and aerodynamic forces, it would contribute little to our main question.

It is evident that wing deformation and alterations in wing kinematics change air flows and thus forces and moments. In an insect both parameters continuously vary throughout the stroke cycle and in response to external forces and sensorimotor control. In this light, all numerical studies on flapping flight are limited in one or the other way because they reduce the number of parameters that are considered in a simulation. Although we recognise the significance of wing deformation, our approach follows the approaches of multiple comparable studies that were previously published on the effect of

corrugation in rigid wings, such as dragonfly [32-40], bumblebee [41-42], locust [43] and fruit fly wings [44].

By contrast, fluid-structure-interaction (FSI) models are typically used for testing flexibility and deformation in simple elastic wing models [45-47]. A compromise between FSI modelling and rigid wing analysis is the use of predescribed changes in wing deformation during flapping for simulation without using FSI modelling [48-53]. Strictly speaking these wing deformations are only valid for flow conditions at one specific flight condition and kinematic pattern. Moreover, as wake structure depends not only on the actual wing stroke but also on previous stroke cycles (wake history), the latter approach is also limited that is similar to rigid wing analyses.

5. Power estimation and efficiency

Muscle mass-specific aerodynamic power requirements for wing flapping was derived from instantaneous local forces $\underline{F}$ (F_x, F_y, F_z) and wing velocity $\underline{u}$ (u_x, u_y, u_z), divided by the fly's flight muscle mass m_{muscle} [54-55]. The latter parameter was approximated by $\frac{1}{3}$ body mass (Table S1). Mass-specific power P^*_{aero} equals to:

$$P^*_{aero} = m^{-1}_{muscle} \int \underline{u}\, d\underline{F}\,. \qquad \text{(eq. S7)}$$

Figure-of-merit for an entire stroke cycle equals Rankine-Froude efficiency η_{RF} and was calculated from the mass-specific theoretical minimum of induced power requirements for flight, i.e.:

$$P^*_{ind} = F_Z m^{-1}_{muscle} \left(\frac{F_Z}{2\rho A_0} \right)^{-0.5}, \qquad \text{(eq. S8)}$$

with A_0 the idealized actuator disk, ρ the air density, and F_z the vertical force in the global frame of reference. Area A_0 swept by one flapping wing equals to the circular sector $0.5\Phi R^2$, with Φ the stroke amplitude and R the wing length. Rankine - Froude efficiency ε *is,*

$$\varepsilon = \frac{P^*_{ind}}{P^*_{aero}}. \qquad \text{(eq. S9)}$$

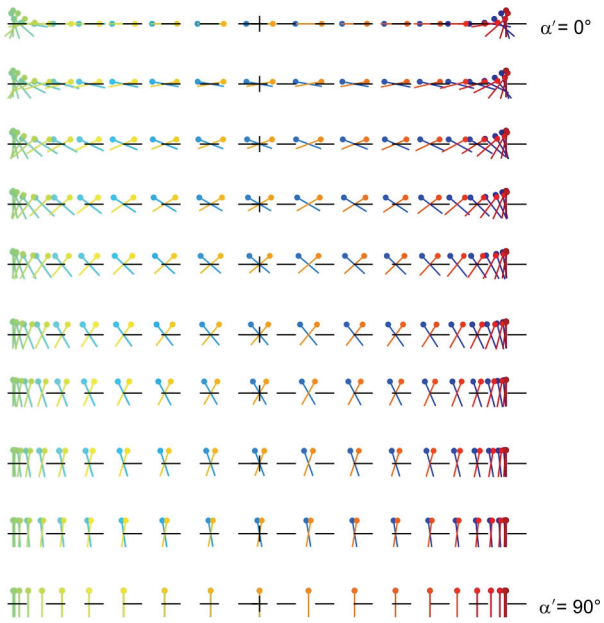

Figure S5. Wing kinematics used for simulations in figures 6 and 7. Stroke plane is horizontal and the wing's angle of attack during the upstroke is equal to the angle during the downstroke. α', the wing's morphological angle of attack.

6. Wing kinematics used for Rakine-Froude efficiency estimation

The simulation data shown in figures 6 and 7 result from a simplified kinematic pattern, in which we removed stroke plane inclination and free stream flow, and angle of attack was equal during up- and downstroke (Fig. S5). This simulation is similar to hovering flight conditions. Other kinematic parameters were adopted from the simulations as shown in figure 1 and morphological parameters from *Calliphora* (Table S1). We also reduced grid resolution to 452 million grid points (768^3 points) to speed up the computations. Angle of attack ranged from 0° to 90° and was increased in increments of 10°. At 0° (90°) angle of attack, the wing rotated 180° (0°) at the stroke reversals but was horizontal (vertical) during the translation phase (Fig. S5).

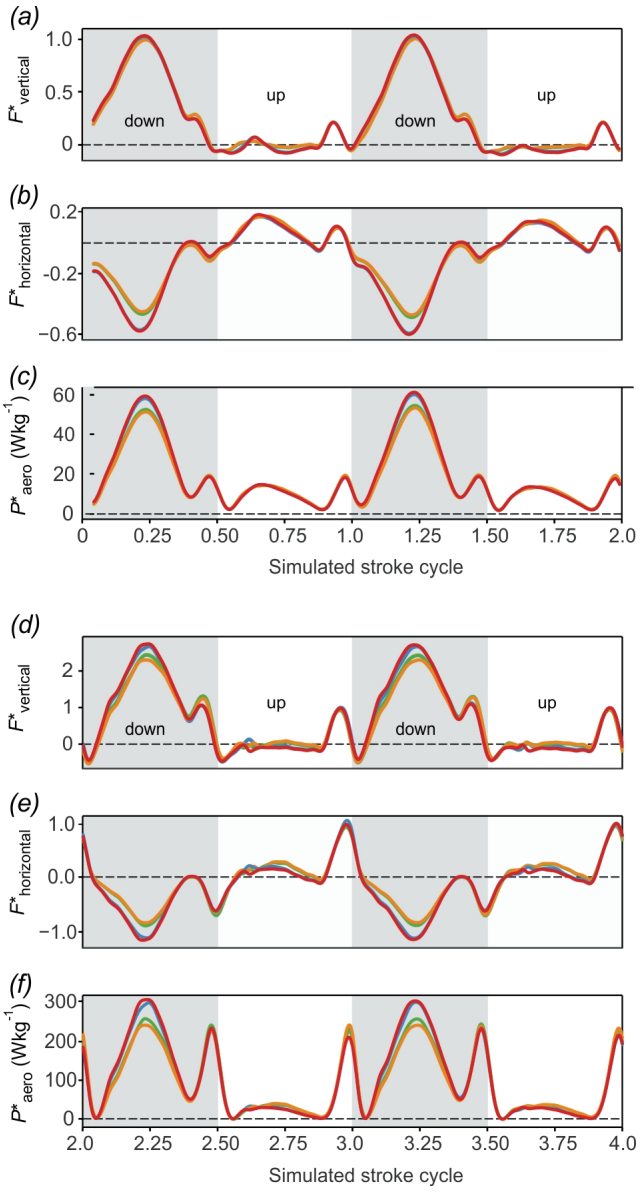

Figure S6. Vertical and horizontal forces, and aerodynamic power requirements produced by natural wings of (*a-c*) *Drosophila* and (*d-f*) *Musca*. $F^*_{vertical}$, instantaneous body-mass specific vertical force in the global frame of reference; $F^*_{horizontal}$, instantaneous body-mass specific horizontal force equal to thrust; P^*_{aero}, instantaneous flight muscle mass-specific aerodynamic power. Red, natural wing; blue, cambered wing; green, corrugated wing; orange, flat wing.

7. Time evolution of forces and aerodynamic power

Instantaneous vertical and horizontal forces, and aerodynamic power requirements for wing flapping were rather similar in all fly species. Thus, in the main text we only show the time evolution for wings of *Calliphora*. The corresponding traces for *Drosophila* and *Musca* are shown in figure S6. In contrast to *Musca* and *Calliphora*, wing models of *Drosophila* did not produce sufficient lift to fully compensate body weight. These differences may result from various factors, such as wing shape, location of the rotational axis, and also Reynolds number.

References

[1] Muijres, F.T., Elzinga, M.J., Melis, J.M. & Dickinson Michael, H. 2014 Flies evade looming targtes by excecuting rapid visually directed banked turns. *Science* **344**, 172-177. (doi:10.1126/science.1248955).

[2] Dickinson, M.H. & Muijres, F.T. 2016 The aerodynamics and control of free flight manoeuvres in *Drosophila*. *Phil. Trans. R. Soc. Lond. B* **371**, 20150388. (doi:10.1098/rstb.2015.0388).

[3] Fry, S.N., Sayaman, R. & Dickinson, M.H. 2005 The aerodynamics of hovering flight in *Drosophila*. *J. Exp. Biol.* **208**, 2303-2318.

[4] Dickinson, M.H., Lehmann, F.-O. & Sane, S. 1999 Wing rotation and the aerodynamic basis of insect flight. *Science* **284**, 1954-1960.

[5] Shishkin, A., Schützner, P., Wagner, C. & Lehmann, F.-O. 2012 Experimental quantification and numerical simulation of unsteady flow conditions during free flight maneuvers in insects. In *Nature-Inspired Fluid Mechanics* (eds. C. Tropea & H. Bleckmann), pp. 81-99. Berlin Heidelberg, Springer.

[6] Götz, K.G. 1983 Bewegungssehen und Flugsteuerung bei der Fliege *Drosophila*. In *BIONA-report 2* (ed. W. Nachtigall), pp. 21-34. Stuttgart, Fischer.

[7] Heide, G. & Götz, K.G. 1996 Optomotor control of course and altitude in *Drosophila melanogaster* is correlated with distinct activities of at least three pairs of flight steering muscles. *J. Exp. Biol.* **199**, 1711-1726.

[8] Balint, C.N. & Dickinson, M.H. 2001 The correlation between wing kinematics and steering muscle activity in the blowfly *Calliphora vicina*. *J. Exp. Biol.* **204**, 4213-4226.

[9] Tu, M.S. & Dickinson, M.H. 1996 The control of wing kinematics by two steering muscles of the blowfly (*Calliphora vicina*). *J. Comp. Physiol. A* **178**, 813-830.

[10] Nachtigall, W. 1966 Die Kinematik der Schlagflügelbewegungen von Dipteren. Methodische und Analytische Grundlagen zur Biophysik des Insektenflugs. *Zeitschrift für vergleichende Physiology* **52**, 155-211.

[11] Nachtigall, W. & Roth, W. 1983 Correlations between stationary measurable parameters of wing movement and aerodynamic force productin in the blowfly (*Calliphora vicina* R.-D.). *J. Comp. Physiol.* **150**, 251-260.

[12] Balint, C.N. & Dickinson, M.H. 2004 Neuromuscular control of aerodynamic forces and moments in the blowfly, *Calliphora vivina*. *J. Exp. Biol.* **207**, 3813-3838.

[13] Ennos, A.R. 1989 The kinematics and aerodynamics of the free flight of some Diptera. *J. Exp. Biol.* **142**, 49-85.

[14] Nasir, N. 2017 Dynamics of high-speed-resolved wing and body kinematics of freely flying houseflies responding to directed and undirected air turbulence [Dissertation], TU Darmstadt.

[15] Lehmann, F.-O. & Dickinson, M.H. 1997 The changes in power requirements and muscle efficiency during elevated force production in the fruit fly, *Drosophila melanogaster. J. Exp. Biol.* **200**, 1133-1143.

[16] Muijres, F.T., Elzinga, M.J., Iwasaki, N.A. & Dickinson Michael, H. 2015 Body saccades of *Drosophila* consist of stereotyped banked turns. *J. Exp. Biol.* **218**, 864-875. (doi:10.1242/jeb.114280).

[17] Fry, S.N., Sayaman, R. & Dickinson, M.H. 2003 The aerodynamics of free-flight maneuvers in *Drosophila*. *Science* **300**, 495-498.

[18] Lehmann, F.-O. 1998 The scaling of aerodynamic performance in fruit flies. In *Biona-report Motion systems* (eds. R. Blickhan, A. Wisser & W. Nachtigall), pp. 175-176. Stuttgart, Gustav Fischer.

[19] Lehmann, F.-O., Gorb, S., Nasir, N. & Schützner, P. 2011 Elastic deformation and energy loss of flapping fly wings. *J. Exp. Biol.* **214**, 2949-2961.

[20] Lehmann, F.-O. & Pick, S. 2007 The aerodynamic benefit of wing–wing interaction depends on stroke trajectory in flapping insect wings. *J. Exp. Biol.* **210**, 1362-1377.

[21] Ellington, C.P. 1984 The aerodynamics of hovering insect flight. III. Kinematics. *Proc. Roy. Soc. Lond. B* **305**, 41-78.

[22] Dickinson, M.H., Lehmann, F.-O. & Götz, K.G. 1993 The active control of wing rotation by *Drosophila*. *J. Exp. Biol.* **182**, 173-189.

[23] Götz, K.G. & Wandel, U. 1984 Optomotor control of the force of flight in *Drosophila* and *Musca* II. Covariance of lift and thrust in still air. *Biol. Cybern.* **51**, 135-139.

[24] David, C.T. 1978 The relationship between body angle and flight speed in free flying *Drosophila*. *Physiol. Entomol.* **3**, 191-195.

[25] Mronz, M. & Lehmann, F.-O. 2008 The free flight response of *Drosophila* to motion of the visual environment. *J. Exp. Biol.* **211**, 2026-2045.

[26] Hoff, W. 1919 Der Flug der Insekten und Vögel. *Naturwissenschaften* **10**, 159-162.

[27] Bomphrey, R.J., Walker, S.M. & Taylor, G.K. 2009 The typical fligth performance of blowflies: measuring the normal performance envelope of *Calliphora vicina* using a novel corner-cube arena. *PLoS ONE* **4**, e7852. (doi:10.1371/journal.pone.0007852).

[28] Wehmann, H.-N., Heepe, L., Gorb, S.N., Engels, T. & Lehmann, F.-O. 2019 Local deformation and stiffness distribution in fly wings. *Biol. Open* **8**, bio038299.

[29] Maeda, M. & Liu, H. 2013 Ground effect in fruit fly hovering: a three-dimensional computational study. *J. Biomech. Sci. Eng.* **8**, 344-355.

[30] Lehmann, F.-O. 1997 The changes of wing kinematics and power requirements during elevated force production in the genus *Drosophila*. In *Neurobiology - from Membrane to Mind* (eds. N. Elsner & H. Wässle), p. 276. Stuttgart New York, Georg Thieme.

[31] Engels, T., Kolomenskiy, D., Schneider, K., Lehmann, F.-O. & Sesterhenn, J. 2016 Bumblebee flight in heavy turbulence. *Phys. Rev. Lett.* **116**, 028103. (doi:10.1103/PhysRevLett.116.028103).

[32] Vargas, A., Mittal, R. & Dong, H. 2008 A computational study of the aerodynamic performance of a dragonfly wing section in gliding flight. *Bioinspiration & Biomimetics* **3**, 026004.

[33] Kim, W.-K., Ko, J.H., Park, H.C. & Byun, D. 2009 Effects of corrugation of the dragonfly wing on gliding performance. *J. Theor. Biol.* **260**, 523-530.

[34] Levy, D.-E. & Seifert, A. 2009 Simplified dragonfly airfoil aerodynamics at Reynolds numbers below 8000. *Phys. Fluids* **21**, 071901.

[35] Hord, K. & Liang, Y. 2012 Numerical investigation of the aerodynamic and structural characteristics of a corrugated airfoil. *J. Aircraft* **49**, 749-757.

[36] Barnes, C.J. & Visbal, M.R. 2013 Numerical exploration of the origin of aerodynamic enhancements in [low-Reynolds number] corrugated airfoils. *Phys. Fluids* **25**, 115106.

[37] Chen, Y. & Skote, M. 2016 Gliding performance of 3-D corrugated dragonfly wing with spanwise variation. *J. Fluid Struct.* **62**, 1-13.

[38] Flint, T.J., Jermy, M.C., New, T.H. & Ho, W.H. 2017 Computational study of a pitching bio-inspired corrugated airfoil. *Int. J. Heat Fluid Flow* **65**, 328-341.

[39] Shahzad, A., Hamdani, H.R. & Aizaz, A. 2017 Investigation of corrugated wing in unsteady motion. *J. Appl. Fluid Dyn.* **10**, 833-845.

[40] Ansari, M.I. & Anwer, S.F. 2018 Numerical analysis of an insect wing in gliding flight: effect of corrugation on suction side. *FDMP* **14**, 259-279.

[41] Meng, X. & Sun, M. 2011 Aerodynamic effects of corrugation in flapping insect wings in forward flight. *J. Bionic. Eng.* **8**, 140-150.

[42] Feaster, J., Battaglia, F. & Bayandor, J. 2017 A computational study on the influence of insect wing geometry on bee flight mechanics. *Biol. Open* **6**, 1784-1795.

[43] Xiang, J., Du, J., Li, D. & Liu, K. 2016 Aerodynamic performance of the locust wing in gliding mode at low Reynolds number. *J. Bionic. Eng.* **13**, 249-260.

[44] Luo, G. & Sun, M. 2005 The effects of corrugation and wing planform on the aerodynamic force production of sweeping model insect wings. *Acta Mech. Sin.* **21**, 531-541.

[45] Nakata, T. & Liu, H. 2012 A fluid-structure interaction model of insect flight with flexible wings. *J. Comp. Phys.* **231**, 1822-1847. (doi:10.1016/j.jcp.2011.11.005).

[46] Nguyen, T.T., Sundar, D.S., Yeo, K.S. & Lim, T.T. 2016 Modeling and analysis of insect-like flexible wings at low Reynolds number. *J. Fluid Struct.* **62**, 294-317. (doi:10.1016/j.jfluidstructs.2016.01.012).

[47] Tobing, S., Young, J. & Lai, J.C.S. 2017 Effects of wing flexibility on bumblebee propulsion. *J. Fluid Struct.* **68**, 141-157. (doi:10.1016/j.jfluidstructs.2016.10.005).

[48] Du, G. & Sun, M. 2012 Aerodynamic effects of corrugation and deformation in flapping wings of hovering hoverflies. *J. Theor. Biol.* **300**, 19-28. (doi:10.1016/j.jtbi.2012.01.010).

[49] Le, T.Q., Truong, T.V., Tran, H.T., Park, S.H., Ko, J.H., Park, H.C., Yoon, K.J. & Byun, D. 2013 Two- and three-dimensional simulations of beetle hind wing flapping during free forward flight. *J. Bionic. Eng.* **10**, 316-328.

[50] Bode-Oke, A.T., Zeyghami, S. & Dong, H. 2018 Flying in reverse: kinematics and aerodynamics of a dragonfly in backward free flight. *J. R. Soc. Interface* **15**, 20180102.

[51] Chen, S., Li, H., Guo, S., M., T. & Ji, B. 2018 Unsteady aerodynamic model of flexible flapping wing. *Aero. Sci. Tech.* **80**, 354-367.

[52] Walker, S.M., Thomas, A.L.R. & Taylor, G.K. 2009 Deformable wing kinematics in the desert locust: how and why do camber, twist and topography vary through the stroke? *J. R. Soc. Interface* **6**, 735-747. (doi:10.1098/rsif.2008.0435).

[53] Walker, S.M., Thomas, A.L.R. & Taylor, G.K. 2010 Deformable wing kinematics in free-flying hoverflies. *J. R. Soc. Interface* **7**, 131-142.

[54] Ellington, C.P., Berg, C.v.d., Willmott, A.P. & .Thomas, A.L.R. 1996 Leading-edge vortices in insect flight. *Nature* **384**, 626-630.

[55] Usherwood, J.R. & Lehmann, F.-O. 2008 Phasing of dragonfly wings can improve aerodynamic efficiency by removing swirl. *J. R. Soc. Interface* **5**, 1303-1307. (doi:10.1098/rsif.2008.0124).